GEOPHYSICS, VOL. 67, NO. 4 (JULY-AUGUST 2002); P. 1270–1274, 9 FIGS.
10.1190/1.1500389

Finite-difference calculation of direct-arrival traveltimes using the eikonal equation

Le-Wei Mo* and Jerry M. Harris‡

ABSTRACT

Traveltimes of direct arrivals are obtained by solving the eikonal equation using finite differences. A uniform square grid represents both the velocity model and the traveltime table. Wavefront discontinuities across a velocity interface at postcritical incidence and some insights in direct-arrival ray tracing are incorporated into the traveltime computation so that the procedure is stable at precritical, critical, and postcritical incidence angles. The traveltimes can be used in Kirchhoff migration, tomography, and NMO corrections that require traveltimes of direct arrivals on a uniform grid.

INTRODUCTION

Wave propagation in high-frequency asymptotics can be described by the WKBJ Green's function, which consists of traveltimes and amplitudes (Cerveny et al., 1977). In this approximation, the traveltimes satisfy the eikonal equation that relates the gradient of the traveltimes to the slowness of the medium. The amplitudes satisfy the transport equation. We address the problem of numerically solving the eikonal equation for direct-arrival traveltimes. One way of solving the eikonal equation is the method of characteristics (Cerveny et al., 1977). There, the ray equations are solved for the raypaths, or characteristic curves of the eikonal equation, and traveltimes are interpolated from the raypaths to gridpoints. However, ray tracing is a slow procedure and has difficulty penetrating shadow zones (Vidale, 1988). Traveltimes on a uniform grid used in seismic migration can be calculated much more efficiently by solving the eikonal equation using the finite-difference method.

Vidale (1988, 1990) presents an efficient finite-difference scheme that solves the eikonal equation for traveltimes in uniform Cartesian grids. The traveltime computation is carried out by recursively solving rings of an expanding square outward from the source point. However, Vidale's scheme encounters instability when the argument of a square root in the traveltime equation becomes negative. Podvin and Lecomte (1991) dissect wave propagation in a cell into all possible modes of transmission, diffraction, and head waves, resulting in a stable scheme of traveltime calculation. Van Trier and Symes (1991) formulate the traveltime calculation in polar coordinates and allow more densely sampled computations nearer the source. However, mapping the slowness field from Cartesian to polar coordinates and the traveltime field from polar to Cartesian coordinates requires extra computations.

The above finite-difference traveltime calculation schemes all calculate traveltimes of first-arrival waves, which may carry very little energy, e.g., head waves and diffractions (Geoltrain and Brac, 1993). In this paper, we first analyze direct-arrival ray tracing. A direct arrival is a transmitted wave without any part of its propagation path being reflection or diffraction or head wave. Next, we present our procedure to calculate the traveltimes of direct arrivals resulting from a point source. Finally, we show several numerical examples, including results of migrating the Marmousi data set with direct-arrival traveltimes.

DIRECT-ARRIVAL RAY TRACING

Figure 1 is a two-layer velocity model. The source is in the layer of slower velocity. In direct-arrival ray tracing, the incident ray at point C on the interface is at critical incidence, and it generates a critically refracted creeping ray along the velocity boundary. The incident rays to the left of point C, e.g., at point A, are at precritical incidence, and they generate refracted waves in the lower layer. The incident rays to the right of point C, e.g., at point B, are at postcritical incidence: total reflection occurs and transmission ray tracing is stopped. For precritical incident rays, the sine of the refraction angle is <1 and the incident wavefront (traveltime contour $T1$) in the slow layer and the corresponding refracted wavefront in the fast layer are continuous across the velocity interface. For postcritical incident rays, however, the incident wavefront (traveltime contour $T2$) in the slow layer and the refracted wavefront in the fast layer are discontinuous across the velocity interface.

Manuscript received by the Editor August 24, 1999; revised manuscript received December 11, 2001.
*Fairfield Industries, Inc., 14100 Southwest Freeway, Suite 100, Sugar Land, Texas 77478. E-mail: lmo@fairfield.com.
‡Stanford University, Department of Geophysics, Stanford, California 94305.

ALGORITHM

In a 2-D medium, the traveltime of wave propagation is described by the eikonal equation,

$$\left(\frac{\partial t}{\partial x}\right)^2 + \left(\frac{\partial t}{\partial z}\right)^2 = s^2(x, z), \tag{1}$$

which relates the gradient of traveltimes to the slowness of the medium, where (x, z) is the spatial coordinate, t is traveltime, and $s(x, z)$ is slowness (reciprocal of velocity). We parameterize the medium using square cells, with mesh spacing h and constant slowness within a cell (Figure 2). In a square cell when traveltimes at three corners a, b, and c are known, the traveltime at the fourth corner, d, can be computed using a finite-difference method assuming local plane-wave propagation. We use the centered finite-difference operator (Vidale, 1988) to approximate the two differential terms in equation (1) and obtain the traveltime t_d at corner d:

$$t_d = t_a + \sqrt{2(hs)^2 - (t_b - t_c)^2}. \tag{2}$$

Here, s is the slowness in the cell with the grid index of corner d, and t_a, t_b, and t_c are traveltimes at corners a, b, and c respectively.

Equation (2) can only be used for traveltime calculations at precritical incidence, where direct-arrival wavefronts are continuous across an interface and the time difference between the diagonal corners of a square cell is $\sqrt{2}\ hs$ at most. At postcritical incidence, the argument inside the square root becomes negative. One option is to reset the negative number inside the square root to zero (Vidale, 1988, 1990), but this does not conform to physical wave phenomena and produces jitters or instability in the traveltime table. Instead, at postcritical incidence, as in direct-arrival ray tracing, we use the critically refracted creeping ray along the velocity boundary (which is also a direct arrival) to compute traveltime:

$$t_d = \min(t_b, t_c) + hs. \tag{3}$$

Equation (3) is applicable for interfaces of 0° and 90° dip, the dip of the interface being recognized by the minimum designation. (In a discrete velocity model, dipping interfaces are represented by stairways, with sides of 0° and 90° dip.) If, in addition to the slowness model, the dips of the interfaces are also stored, then the traveltimes of critically refracted creeping rays may be obtained accurately by using trigonometric relationships. When the term inside the square root in equation (2) becomes negative at locations not in the neighborhood of an interface, the traveltime at corner d is assigned the larger of those at corners b or c. In doing so, we recognize that rays traveling through slow-velocity sediments are likely to be more energetic than those traveling through high-velocity zones such as salt domes.

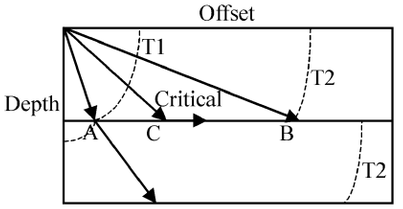

FIG. 1. Direct-arrival transmission ray tracing and wavefronts in a two-layer velocity model. The source is in the layer of slower velocity. Thin, dashed curves represent wavefronts. Note the absence of head-wave arrivals and, therefore, the discontinuity in traveltimes across the interface at postcritical incidence.

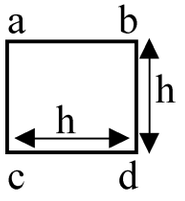

FIG. 2. In a square cell with dimension h and constant slowness s, when traveltimes at three corners are known, the traveltime at the fourth corner can be calculated. Edge ab may be oriented horizontally or vertically.

Computation order

At first, all gridpoints of the traveltime table are assigned a value larger than any possible valid traveltime (this helps in locating local traveltime minima at the two ends of a traveltime computation front edge). The traveltime computation is initialized by using straight raypaths in a square of constant velocity surrounding the source. A square with side $3h$ is chosen here for the initialization. Traveltime computations are then carried out recursively in the order of expanding squares (Figure 3).

The filled squares in the figure indicate gridpoints for which the traveltimes have been calculated. These traveltimes are used to compute traveltimes to gridpoints at the next outer ring (the hollow squares).

When calculating a new ring of traveltimes, computations proceed sequentially on the four edges. (When the source is on the surface of the earth, the top edge need not be computed.) To initialize computation at an edge, the inner edge is first examined in a loop from one end to the other to locate points

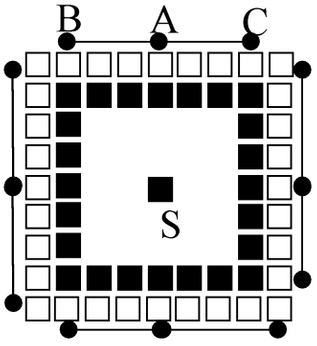

FIG. 3. Computation layout; S is the source point. Traveltime computation proceeds sequentially on the four edges: top, right, bottom, and left. Each edge is divided into two segments separated by the traveltime local minimum closest to the source. Black circles joined by straight lines indicate the two ends of a segment.

of local minimum traveltime. The traveltime t_d to a point on the outer ring directly outside a local minimum is computed as (Vidale, 1988)

$$t_d = t_a + \sqrt{(hs)^2 - 0.25(t_b - t_c)^2}. \quad (4)$$

Here, t_a is the local minimum traveltime in the inner edge, t_b and t_c are the traveltimes at its inner edge neighbors, and s is slowness at corner d. If the argument inside the square root of equation (4) is negative, the traveltime at node d is computed as

$$t_d = t_a + hs. \quad (5)$$

At the next stage, equations (2) and (3) are applied to compute traveltimes sequentially on the four edges. Each edge is divided into two segments separated by the traveltime local minimum closest to the source (Figure 3). For example, in Figure 3 the top edge is divided into segments AB and AC. Point A is the local traveltime minimum closest to the source, which may deviate away from the center of the edge when velocity varies laterally. The traveltime calculation on each segment is done in two loops. In each loop, corners a and b of the square cell (Figure 2) are in the inner edge; corners c and d are in the outer edge. The traveltime calculation is done in upwind order, i.e., $t_a < t_b$. The first loop progresses from B to A, computing traveltimes of incoming waves (traveltimes increase inward). The second loop progresses from A to B, computing traveltimes of outgoing waves (traveltimes increase outward). For a point outside an inner-edge local traveltime maximum, the traveltime computed by the incoming loop (the first loop) is replaced by the traveltime computed by the outgoing loop. The reason is that the direct arriving wave is generally an outgoing wave; for example, looking ahead to Figure 5 at offset 6 km, the direct arrival is propagating down and away from the source, whereas the head wave is propagating up and toward the source. Computations continue to the edges of the model, completely filling the traveltime table.

EXAMPLES

Figure 4 shows traveltime contours of the direct arrival in a velocity model with a high-velocity quadrant superimposed on a velocity trend that increases linearly with depth.

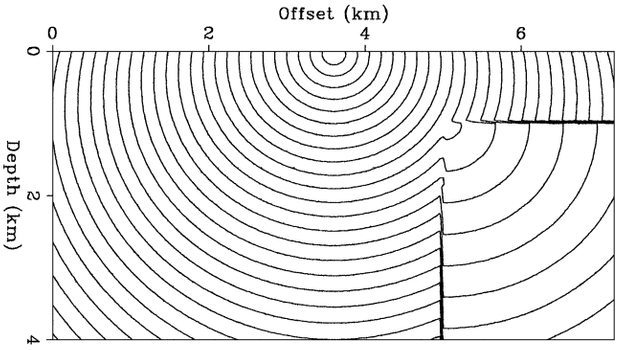

FIG. 4. Traveltime contours of a direct arrival at 0.1 s interval in a velocity model with a high-velocity quadrant.

Figure 5 shows the overlay of the snapshot wavefield computed by finite-difference wave equation modeling and the corresponding traveltime contour at 1.5 s. Notice that the traveltime contour coincides closely with the wavefront of the direct arrival, as opposed to the first-arrival critical refraction (head wave).

Time migration

Both poststack and prestack time migration involve evaluating the NMO equation in a 1-D velocity model. This NMO equation is not accurate for long offset (Causse et al., 2000) because it does not take into account ray bending at velocity interfaces. Our method can compute accurate traveltimes for all offsets. Additionally, where there is no reflector dip $>90^\circ$ and therefore no turning wave, the method can be simplified greatly. The self-explanatory Fortran code is given in the Appendix.

Figure 6 shows traveltime contours in a 1-D model with large-velocity variations (Causse et al., 2000). Thickness in meters and interval velocity in meters per second of the layers, from shallow to deep, are (250, 1500), (400, 2000), (600, 2400), (200, 2800), (500, 3200), and (550, 3600). Note that head-wave traveltimes are not present. A traveltime map such as this, which describes wave propagation accurately for all offsets, can be used in NMO correction and prestack time migration (Kim and Krebs, 1993) after converting depth to time.

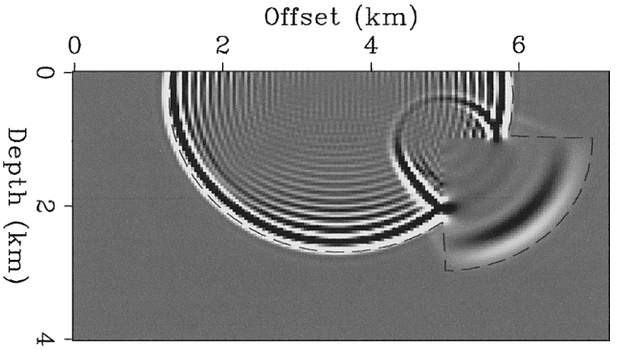

FIG. 5. Overlay of wave-equation modeling snapshot waveform and corresponding traveltime contour at 1.5 s for the same velocity model as Figure 4.

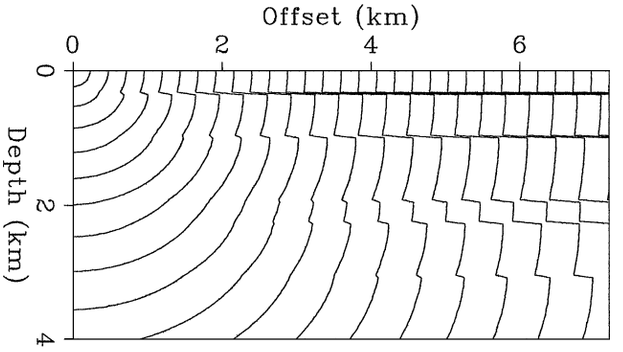

FIG. 6. Traveltime contours of a direct arrival at 0.1 s interval in a 1-D model containing large velocity variations.

Depth migration

We tested our traveltime computation method on the Marmousi synthetic data set (Bourgeois et al., 1991). This data set was generated by 2-D acoustic wave equation modeling using the finite-difference method. It has 240 shot gathers with 96 traces each. The model is constructed based on a profile of actual geology. Because the velocity model and structure are very complicated, it has since become a popular test data set for advanced migration methods (Audebert et al., 1997; Bevc, 1997). The imaging objective is an oil reservoir in an anticline structure below a series of growth faults that cause rapid lateral velocity variations.

Figure 7 shows a direct-arrival traveltime map overlain on the velocity model. Notice the critically refracted creeping ray traveltimes near the upper surface at 8–9 km. Figure 8 shows the stacked image after prestack Kirchhoff depth migration using direct-arrival traveltimes. The growth faults in the upper part of the section are imaged well; the imaging objective, which is the anticline structure below 2.3 km in depth and between the lateral distance 6 and 7 km, is imaged clearly. Figure 9 shows the Kirchhoff migration image using first-arrival traveltimes. The growth faults are not imaged well, and the target anticline structure is largely absent because the first arrivals carry very little energy (Geoltrain and Brac, 1993).

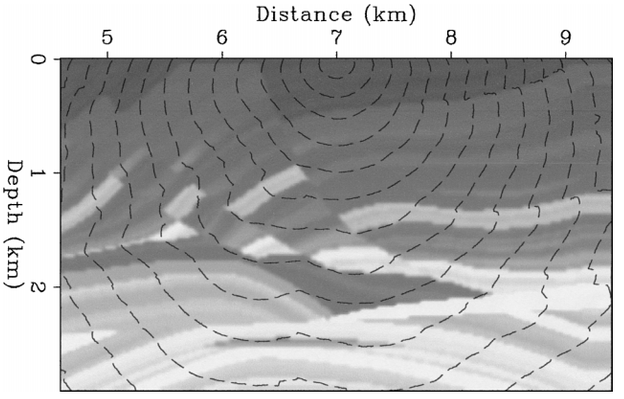

FIG. 7. Overlay of the Marmousi velocity model and direct-arrival traveltime contours.

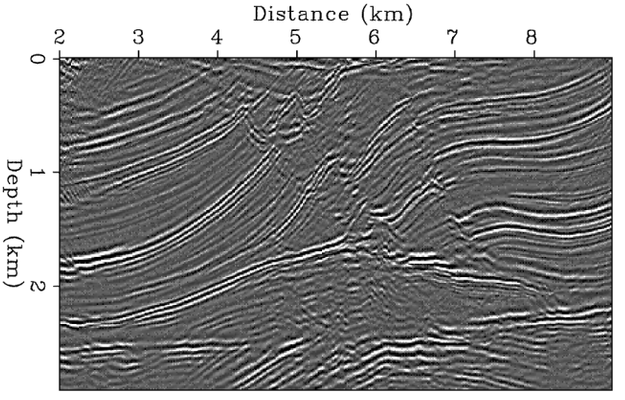

FIG. 8. Marmousi Kirchhoff migration using direct-arrival traveltimes. The target zone at a depth of 2.3 km and a lateral distance of 6 to 7 km is imaged well.

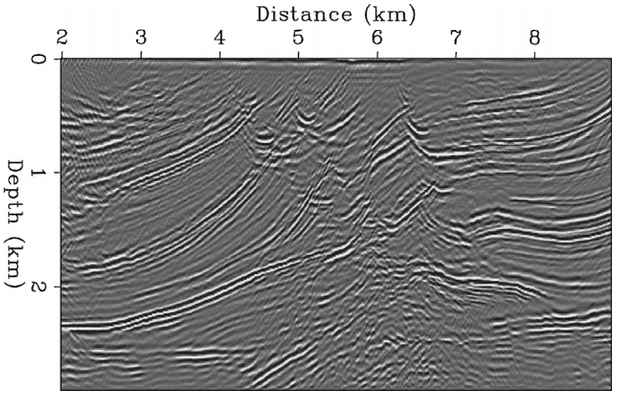

FIG. 9. Marmousi Kirchhoff migration using first-arrival traveltimes. Compare with Figure 8.

CONCLUSIONS

This finite-difference method of solving the eikonal equation successfully computes the traveltimes of direct-arriving waves. The computed traveltimes closely coincide with wavefronts computed by finite-difference wave equation modeling. By incorporating into the traveltime computation some insights in direct-arrival ray tracing and physical wave phenomena—namely, that direct-arrival wavefronts are discontinuous across a velocity interface at postcritical incidence—traveltimes of precritical, critical, and postcritical incidence rays are computed correctly. Additionally, computing the square root of a negative number is avoided so the method is guaranteed to be stable. The computed traveltimes can be used in NMO corrections and in Kirchhoff time and depth migrations.

ACKNOWLEDGMENTS

We thank the sponsors of the Stanford Seismic Tomography project for supporting this research. We also thank the assistant editors Kurt Marfurt and Paul Docherty and the reviewers whose comments and suggestions led to great improvement of the manuscript.

REFERENCES

Audebert, F., Nichols, D., Rekdal, T., Biondi, B., Lumley, D. E., and Urdaneta, H., 1997, Imaging complex geologic structure with single-arrival Kirchhoff prestack depth migration: Geophysics, **62**, 1533–1543.

Bevc, D., 1997, Imaging complex geologic structure with semirecursive Kirchhoff migration: Geophysics, **62**, 577–588.

Bourgeois, A., Bourget, M., Lailly, P., Poulet, M., Ricate, P., and Versteeg, R., 1991, Marmousi, model and data, *in* Versteeg, R., and Grau, G., Eds., The Marmousi experience: Eur. Assoc. Expl. Geophys. workshop on practical aspects of seismic data inversion, Proceedings, 5–16.

Causse, E., Haugen, G. U., and Romme, B. E., 2000, Large-offset approximation to seismic reflection traveltimes: Geophys. Prosp., **48**, 763–778.

Cerveny, V., Molotkov, I. A., and Psencik, I., 1977, Ray method in seismology: Karlova Univercity.

Geoltrain, S., and Brac, J., 1993, Can we image complex structure with first-arrival traveltime?: Geophysics, **58**, 564–575.

Kim, Y. C., and Krebs, J. R., 1993, Pitfalls in velocity analysis using common-offset time migration: 63rd Ann. Internat. Mtg., Soc. Expl. Geophys., Expanded Abstracts, 969–973.

Podvin, P., and Lecomte, I., 1991, Finite difference computation of traveltimes in very contrasted velocity models: A massively parallel

approach and its associated tools: Geophys. J. Internat., **105**, 271–284.
Van Trier, J., and Symes, W. W., 1991, Upwind finite-difference calculation of traveltimes: Geophysics, **56**, 812–821.
Vidale, J., 1988, Finite-difference calculation of travel times: Bull. Seis. Soc. Am., **78**, 2062–2076.
——— 1990, Finite-difference calculation of traveltimes in three dimensions: Geophysics, **55**, 521–526.

APPENDIX

FORTRAN PROGRAM TO COMPUTE TRAVELTIMES FOR NMO AND TIME MIGRATION

```
real s(nz),t(nz,nx),h #slowness, 2-D traveltime table, grid spacing
t(1,1)=0 # source location
do ix=2,nx # horizontal ray along surface
   t(1,ix)=t(1,ix-1)+s(1)*h
enddo
do iz=2,nz # vertical ray below source
   t(iz,1)=t(iz-1,1)+s(iz)*h
enddo
do iz=2,nz # now fill the remainder of the table
do ix=2,nx # computation layer one after another
   tmp=2*s(iz)*s(iz)*h*h
   tmp=tmp-(t(iz-1,ix)-t(iz,ix-1))* (t(iz-1,ix)-t(iz,ix-1))
   if (tmp .ge. 0.) then # pre-critical
      t(iz,ix)=t(iz-1,ix-1)+sqrt(tmp)
   else # horizontal creeping ray
      t(iz,ix)=t(iz,ix-1)+s(iz)*h
   endif
enddo
enddo
```